

A Regioselectively Oxidized 2D Bi/BiOx Lateral Nano-Heterostructure for Hypoxic Photodynamic Therapy

Meng Qiu, Dou Wang, Hao Huang, Teng Yin, Wenli Bao, Bin Zhang, Zhongjian Xie, Ni Xie, Zongze Wu, Chenchen Ge, Qi Wang, Meng Gu, Hilliard L. Kutscher, Liping Liu, Shiyun Bao,* Paras N. Prasad,* and Han Zhang*

Optoelectronic science and 2D nanomaterial technologies are currently at the forefront of multidisciplinary research and have numerous applications in electronics and photonics. The unique energy and optically induced interfacial electron transfer in these nanomaterials, enabled by their relative band alignment characteristics, can provide important therapeutic modalities for healthcare. Given that nano-heterostructures can facilitate photoinduced electron–hole separation and enhance generation of reactive oxygen species (ROS), 2D nano-heterostructure-based photosensitizers can provide a major advancement in photodynamic therapy (PDT), to overcome the current limitations in hypoxic tumor microenvironments. Herein, a bismuthene/bismuth oxide (Bi/BiOx)-based lateral nano-heterostructure synthesized using a regioselective oxidation process is introduced, which, upon irradiation at 660 nm, effectively generates $^1\text{O}_2$ under normoxia but produces cytotoxic $\bullet\text{OH}$ and H_2 under hypoxia, which synergistically enhances PDT. Furthermore, this Bi/BiOx nano-heterostructure is biocompatible and biodegradable, and, with the surface molecular engineering used here, it improves tumor tissue penetration and increases cellular uptake during *in vitro* and *in vivo* experiments, yielding excellent oxygen-independent tumor ablation with 660 nm irradiation, when compared with traditional PDT agents.

1. Introduction

Cancer is the second leading cause of death worldwide.^[1] Consequently, the research and development of anticancer therapeutic agents and approaches to improve curative effects and reduce dose-limiting side effects is ongoing. One such therapeutic approach is photodynamic therapy (PDT), as it can kill targeted cancer cells via cytotoxic reactive oxygen species (ROS), mostly singlet oxygen ($^1\text{O}_2$), which are generated by light absorption in a photosensitizer (PS) in the presence of oxygen.^[2] This mechanism of PDT is often referred to as type II. PDT offers specific spatiotemporal selectivity and minimal invasiveness and is clinically approved for a wide range of customized precision medical treatments, especially for malignant cancers.^[3–5] However, the widespread clinical use of PDT is limited by the hypoxic microenvironment that is often found in tumors, as it suppresses the

M. Qiu, H. Huang, T. Yin, W. Bao, B. Zhang, Z. Xie, N. Xie, H. Zhang
Shenzhen Second People's Hospital The First Affiliated Hospital of
Shenzhen University
Key Laboratory of Optoelectronic Devices
Systems of Ministry of Education
Guangdong Province Institute of Microscale Optoelectronics
Shenzhen University
Shenzhen 518060, P. R. China
E-mail: hzhang@szu.edu.cn

M. Qiu
Key Laboratory of Marine Chemistry Theory and Technology
Ministry of Education
Ocean University of China
Qingdao 266100, P. R. China

D. Wang, Z. Wu, C. Ge, L. Liu, S. Bao
Shenzhen People's Hospital (The First Affiliated Hospital)
Southern University of Science and Technology
Shenzhen 518020, P. R. China
E-mail: bao.shiyun@szhospital.com

 The ORCID identification number(s) for the author(s) of this article can be found under <https://doi.org/10.1002/adma.202102562>.

Q. Wang, M. Gu
Department of Materials Science and Engineering
South University of Science and Technology
Shenzhen 518055, P. R. China

H. L. Kutscher, P. N. Prasad
Institute for Lasers, Photonics, and Biophotonics
Department of Chemistry
University at Buffalo
The State University of New York
Buffalo, NY 14260, USA
E-mail: pnprasad@buffalo.edu

H. L. Kutscher
Department of Medicine
University at Buffalo
The State University of New York
Buffalo, NY 14203, USA

H. L. Kutscher
Department of Anesthesiology
University at Buffalo
The State University of New York
Buffalo, NY 14203, USA

DOI: 10.1002/adma.202102562

generation of $^1\text{O}_2$ from PSs, thereby decreasing the efficiency of PDT treatments.^[6–8]

Various strategies have been utilized to alleviate hypoxia, such as strengthening the oxygen supply within the tumor region,^[7,9] photothermally enhancing PDT,^[10–12] integrating PSs with prodrugs that are activated under hypoxic conditions,^[8] as well as enhancing the tumor cell-targeting capability of PSs.^[13,14] Nevertheless, the abovementioned strategies have not solved the hypoxia-related issues completely, and may even cause other complications and side effects. Therefore, novel efficient PSs that generate ROS beyond $^1\text{O}_2$ (i.e., via an O_2 -independent mechanism) and that have excellent biocompatibility are highly desirable. The bismuthene/bismuth oxide (Bi/BiOx) nano-heterostructures developed in this work may have great clinical PDT application as they can make use of an electron-transfer process that not only interacts with ground state O_2 to generate superoxide anions ($\text{O}_2^{\bullet-}$), but also interacts with H_2O to generate hydroxyl radicals ($\bullet\text{OH}$), respectively, both of which are cytotoxic. Therefore, type I PDT, which utilizes these ROS, can take place even in hypoxic environments without the participation of oxygen.

Emerging 2D nanomaterials can be tailored precisely and then combined into vertical or lateral nano-heterostructures with customized band alignments to form Schottky-type heterojunctions. Upon optical excitation, these junctions can yield the efficient separation of electrons and create holes in different material nanodomains. Furthermore, as the conduction band minimum and Fermi energy of the Schottky-type heterojunctions are located on different components, the photoinduced electrons and holes can be spatially separated. Consequently, the lateral nano-heterojunctions are beneficial as they can boost the electron-transfer efficiency, thereby facilitating type I PDT to generate ROS such as $\bullet\text{OH}$.

Recently, 2D bismuthene has demonstrated excellent biocompatibility and has been utilized as a computed tomography contrast agent,^[15,16] as well as a photoacoustic and photothermal agent.^[17] Nevertheless, few studies have demonstrated the effectiveness of 2D bismuthine as an effective PDT agent. The potential biomedical application has motivated our development of 2D bismuthene for efficient PDT in this investigation. We have thus demonstrated that a Bi/BiOx-based lateral nano-heterostructure, fabricated by a hydrothermal regioselective oxidation method, is capable of robust ROS generation under irradiation in an O_2 -independent environment (Figure 1). In addition to the type II PDT process initiated by the energy transfer from photoexcited Bi in the core to molecular O_2 in the ground to generate $^1\text{O}_2$, type I PDT was also activated by an electron transfer process under light irradiation, benefiting from suitable band alignment in the Bi/BiOx lateral nano-heterostructure. The underlying mechanism of the photocatalytic process was investigated, and it was revealed that the hydroxide ions from the aqueous medium were oxidized to $\bullet\text{OH}$ on the anodic valence band of BiOx, while O_2 and H^+ were reduced to $\text{O}_2^{\bullet-}$ and H_2 under normoxia and hypoxia, respectively, on the cathodic Fermi level of the Bi. Therefore, the Bi/BiOx lateral nano-heterostructure could generate ROS by irradiation under both normoxic and hypoxic tumor conditions.

After surface molecular engineering that conjugated the Bi/BiOx nano-heterostructures to dicarboxyl-poly(ethylene

glycol) (HOOC-PEG-COOH), it was found that the resulting nanostructure cage could infiltrate the tumor tissue through transcytosis more efficiently in an acidic tumor microenvironment.^[18–20] Furthermore, in vitro and in vivo experiments demonstrated that this Bi/BiOx lateral nano-heterostructure has excellent oxygen-independent tumor ablation capability when compared to conventional type II PDT agents. Such a novel therapeutic nanoplatform with excellent PDT efficiency and inherent biosafety creates a new area for research which may help to improve the future of precision medicine.

2. Results and Discussion

2.1. Characterization of the Bi/BiOx Lateral Nano-Heterostructure

Transmission electron microscopy (TEM) clearly demonstrated the presence of Bi nanosheets (BiNSs) and Bi/BiOx lateral nano-heterostructures before and after the regioselective oxidation process (Figure 2a,b). Both BiNSs and Bi/BiOx nano-heterostructures exhibited regular hexagonal nanosheets with a mean diameter of ≈ 55 nm. The low-magnification TEM images of BiNSs and Bi/BiOx lateral nano-heterostructure were shown in Figure S1 (Supporting Information). The dynamic light scattering (DLS) size distributions of the BiNSs and Bi/BiOx nano-heterostructures are shown in Figure S4 (Supporting Information). The structures were further investigated using atomic high-angle annular dark-field scanning transmission electron microscopy (HAADF-STEM) (Figure 2e). The hexagonal nanosheet structure displayed along the [001] zone axis and a layer structure displayed along the lateral direction were consistent with the $R\bar{3}m$ structure of Bi. The lattice spacing along the lateral direction was 0.4 nm, corresponding to the [003] planes of the Bi (Figure 2e inset). The selected-area electron diffraction (SAED) pattern (Figure S3f, Supporting Information) reveals that the Bi/BiOx nano-heterostructure is highly crystalline in the core region, maintaining the inherent structure of the bulk Bi. The statistical analysis of the $n = 100$ Bi/BiOx nano-heterostructure, imaged by TEM and atomic force microscopy (AFM) (Figure 2b,c), found that the mean lateral size was 56.2 ± 25.8 nm and the average thickness was 5.9 ± 4.2 nm (Figure 2d), and the layered structures can clearly be seen in Figure 2e inset. After surface molecular engineering modifications, the mean size distribution of the dicarboxylic poly(ethylene glycol)-coated nano-heterostructure, namely Bi/BiOx nanospheres (Bi/BiOx@NSPs), increased from 60 to 104 nm, as measured using DLS (Figure 2o). The TEM and AFM images of the Bi/BiOx@NSPs with surface modifications are shown in Figures S5 and S6 (Supporting Information).

The elemental distributions of Bi and O in the Bi/BiOx nano-heterostructure were characterized using STEM-energy-dispersive X-ray spectroscopy (STEM-EDS) mapping (Figure 2f,g and Figure S3a–c (Supporting Information)), where the Bi (red), O (yellow), and merged images confirmed the presence of a BiOx edge layer around the Bi core. The element distribution profile also demonstrated that Bi was dominant in the core region, whereas O was dominant in the edge region (Figure S3d, Supporting Information).

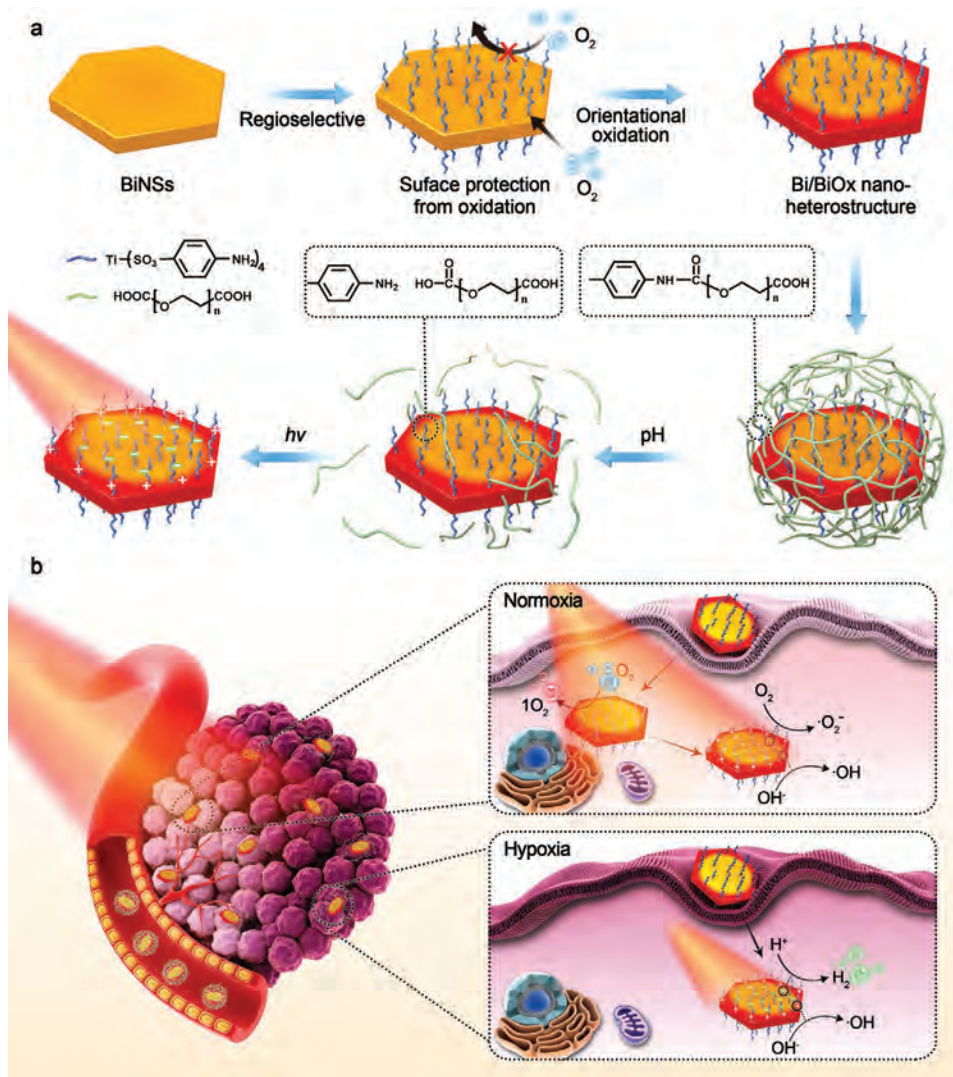


Figure 1. Lateral nano-heterostructure synthesis and PDT treatment schematic. a) Preparation workflow for the Bi/BiOx lateral nano-heterostructure and photoinduced charge separation characteristics. b) Improved deep tumor penetration of the Bi/BiOx lateral nano-heterostructure in an acidic tumor microenvironment by virtue of a positively charged surface and smaller nanoparticle size to enhance transcytosis. The working principle of the Bi/BiOx lateral nano-heterostructure for enhanced PDT with irradiation under both normoxia and hypoxia.

Raman peaks of the Bi nanosheet exhibited nearly identical first-order Raman modes of the in-plane E_g and the out-of-plane A_{1g} vibration modes at 65.6 and 91 cm^{-1} , respectively, acquired using 1064 nm excitation. This confirms that the intrinsic nature of the Bi structure is maintained during the exfoliation process (Figure 2i). After the regioselective hydrothermal oxidation process, the as-prepared Bi/BiOx heterostructure showed six additional Raman peaks at 118, 135, 176, 203, 300, and 432 cm^{-1} . These peaks were consistent with those reported for Bi_2O_3 ,^[21] and indicated that the edge of the Bi nanosheet was oxidized to BiOx during the hydrothermal process. The crystal structures of the Bi and Bi/BiOx nano-heterostructures were further confirmed by X-ray diffraction (XRD). The representative diffraction peaks of Bi and Bi/BiOx nano-heterostructure could be well indexed to coincide with the standard rhombohedral phase of Bi (JCPDS card No. 44-1246), indicating that the BiOx phase had an amorphous structure (Figure 2j). X-ray photoelectron

spectroscopy (XPS) was performed to determine the chemical components of the Bi/BiOx heterostructure (Figure 2k,l). The Bi/BiOx nano-heterostructure showed 4f 7/2 and 4f 5/2 doublets at 158 and 164 eV, respectively. The lower energy sets belonged to Bi in the inner core, whereas the higher energy sets belonged to the oxidation state of BiOx in the outer shell.

As the acidic tumor microenvironment could hydrolyze the amide bond of the PEG polymer to generate amine groups, the Bi/BiOx@NSPs could undergo charge transfer once entering the tumor tissue.^[18,19] The phosphate-buffered saline (PBS) suspension solution of the as-prepared Bi/BiOx@NSPs with a pH of 7.4 was negatively charged, while when Bi/BiOx@NSPs were suspended in a PBS solution with a pH of 6.0, their zeta potential became positive (Figure 2m,n). The mean size distribution of Bi/BiOx@NSPs, as determined by DLS, was reduced dramatically from 104 to 60 nm in the acidic solution, which was beneficial for tumor penetration (Figure 2o,p).^[18]

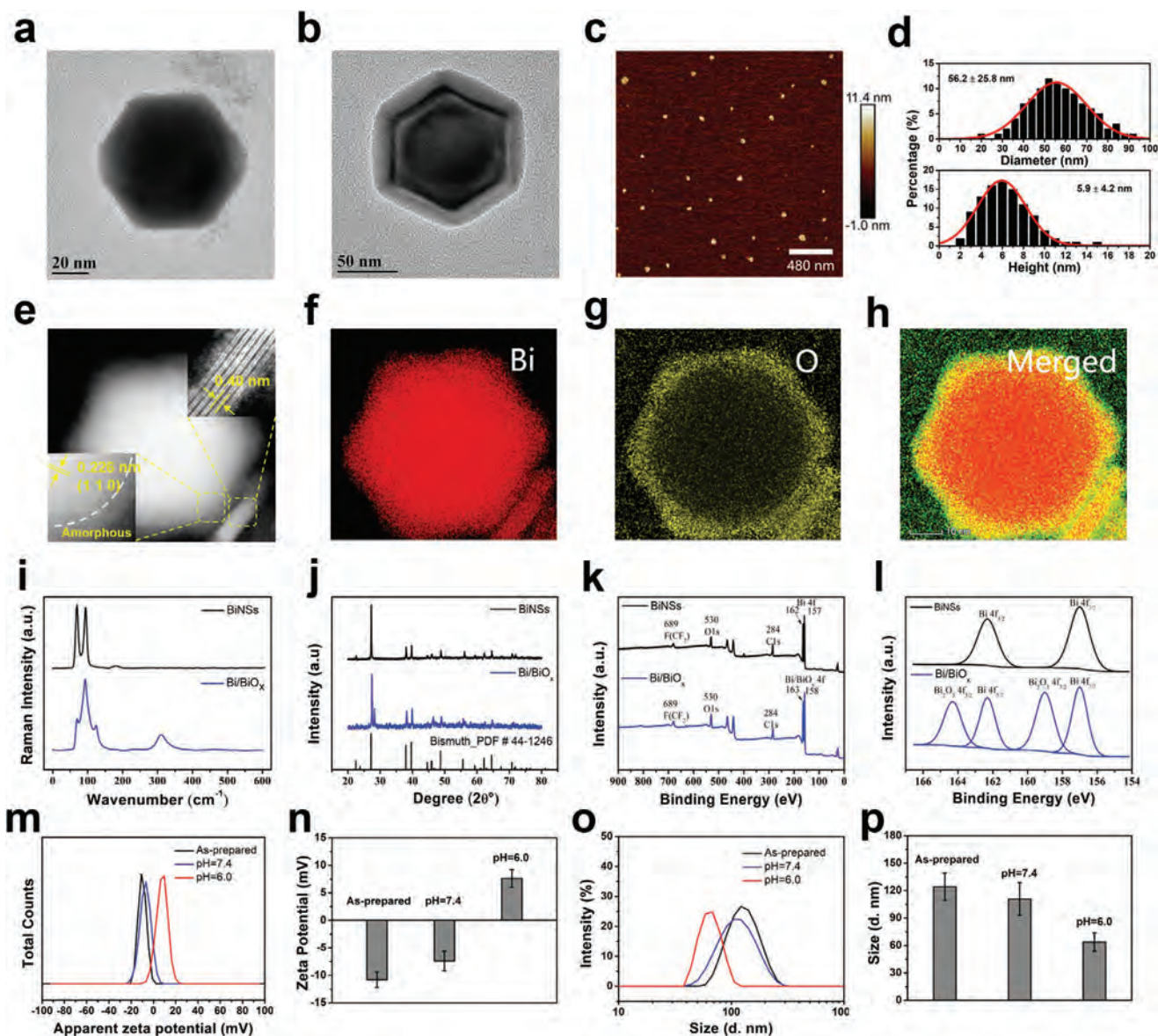


Figure 2. Characterization of the Bi lateral nano-heterostructure. a,b) TEM images of the BiNSs (a) and Bi/BiOx lateral nano-heterostructure (b). c) AFM image of Bi/BiOx lateral nano-heterostructure. d) Statistical analysis of the lateral sizes and heights for 100 samples, as determined by TEM and AFM, respectively. e) HRTEM of the Bi/BiOx lateral nano-heterostructure. f–h) STEM–EDS mapping of the Bi/BiOx lateral nano-heterostructure. i) Raman spectra of the BiNSs and Bi/BiOx lateral nano-heterostructure acquired at the 532 nm excitation wavelength, j) XRD pattern of BiNSs and the Bi/BiOx lateral nano-heterostructures; the black lines show the corresponding standard pattern of bismuth (JCPDS card No. 44-1246). k,l) XPS scan of the BiNSs and Bi/BiOx lateral nano-heterostructures, respectively. m,n) DLS zeta potential of Bi/BiOx@NSPs under a normal or acidic tumor microenvironment, respectively. o,p) DLS size distribution of Bi/BiOx@NSPs under a normal or acidic tumor microenvironment, respectively.

2.2. Photocatalytic Performance of ROS Generation

To establish a Schottky-type band alignment for effective type I PDT performance, in situ ultraviolet photoelectron spectroscopy (UPS) was used to examine the electron structure of the interface for the Bi/BiOx lateral heterostructure (Figure 3b). The working function of the Bi/BiOx was determined to be -4.4 eV using the difference between the photon energy (21.22 eV) and the cutoff energy (16.82 eV) (Figure 3c). The valence band maximum relative to the Fermi level of Bi/BiOx was determined to be 1.61 eV by linearly extrapolating the onset energy in the

low-energy region (Figure 3d). The bandgaps of Bi/BiOx were measured using a Tauc plot of the UV–vis spectra and found to be 1.83 eV (Figure 3e). Therefore, the metallic Bi and semiconductor BiOx formed a Schottky-type junction, which could have an intense photovoltaic effect to facilitate the generation of electrons and holes on each side.

The proposed photocatalytic mechanism is shown in Figure 3a. For the cathodic reaction under normoxic conditions, O_2 is reduced to $O_2^{\cdot-}$ by accepting one electron, and the required energy barrier is easily overcome with the bandgap based on the chemical potential value of $O_2/O_2^{\cdot-}$. The H^+ is

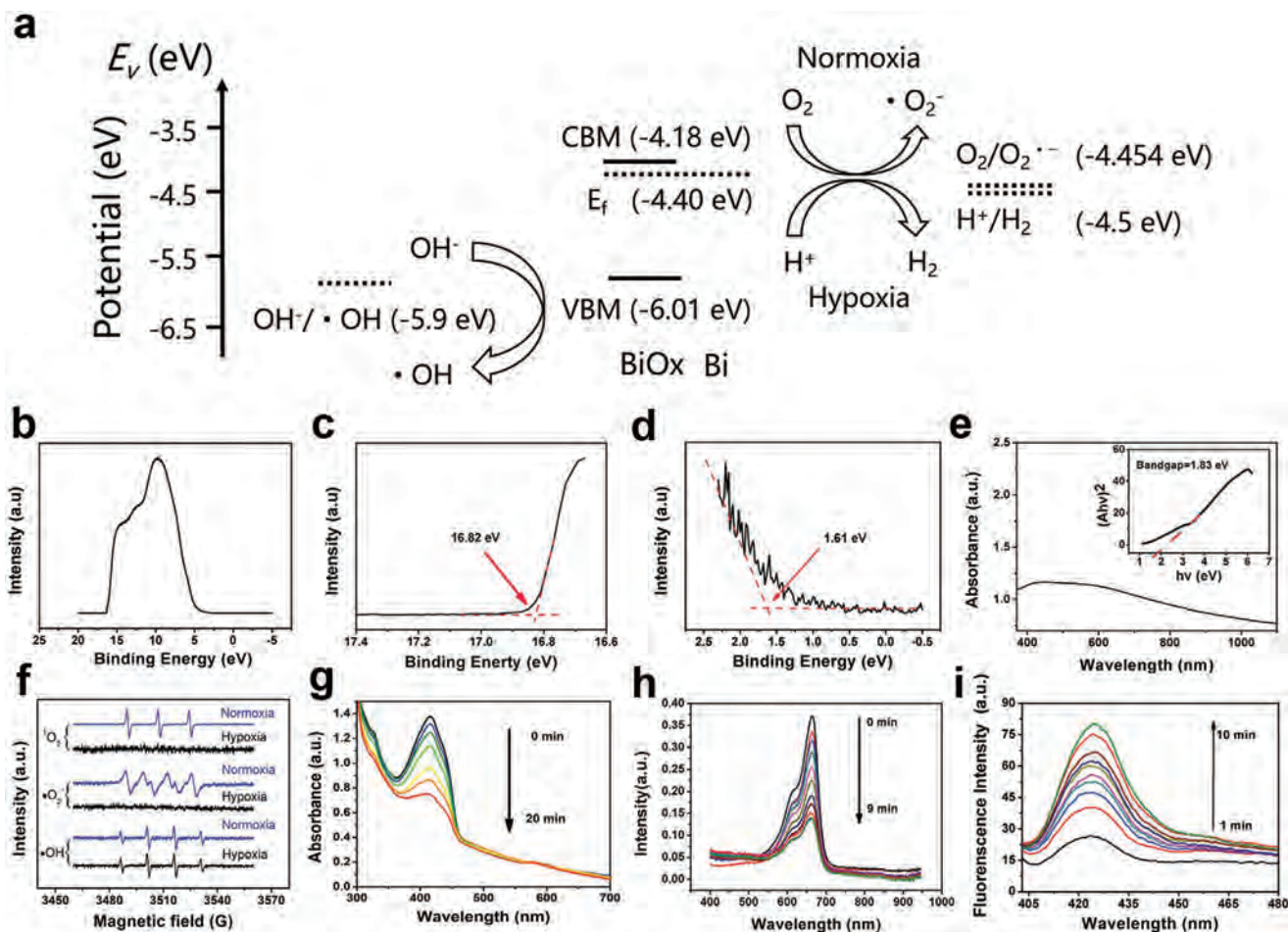


Figure 3. Band structure and the ROS generating ability of the Bi/BiOx nano-heterostructure. a) The working principle of Bi/BiOx lateral nano-heterostructure for PDT and the corresponding energy level alignment for ROS and hydrogen generation. b–d) UPS spectra of the Bi lateral nano-heterostructure. e) Tauc plot from the UV–vis absorption spectra (inset) of the Bi/BiOx. f) $\cdot O_2$, $\cdot O_2^-$, and $\cdot OH$ generation from the Bi/BiOx lateral nano-heterostructure characterized by ESR spectra under hypoxic and normoxic conditions. g) $\cdot O_2$ generation from the Bi/BiOx lateral nano-heterostructure characterized by a change in the absorption spectra in the presence of 1,3-diphenylisobenzofuran (DPBF). h) H_2 generation from the Bi/BiOx lateral nano-heterostructure characterized by a change in the absorption spectra in the presence of methylene blue–Pt. i) $\cdot OH$ generation from the Bi/BiOx lateral nano-heterostructure characterized by a change in fluorescence spectra in the presence of terephthalic acid (TA).

reduced to H_2 by accepting one electron under hypoxic conditions. For the anodic reaction, the dominant process is the transformation of OH^- to $\cdot OH$ through the combination with the hole from the valence band of BiOx (Figure 3a), under both normoxic and hypoxic conditions.^[22,23] Both cathodic and anodic reactions match well with the band alignment in the Bi/BiOx heterostructure. By contrast, for black phosphorus nanosheets, only the conducting band met the requirement of the cathodic reaction, while the valence band (–4.7 to –5.4 eV for multilayer to monolayer black phosphorous nanosheets) was too high to meet the requirement of the anodic reaction.^[24,25]

Electron spin resonance (ESR) was used to directly identify the ROS species generated by the Bi/BiOx lateral nano-heterostructure. The ESR signal for the Bi/BiOx lateral nano-heterostructure in the presence of 4-amino-2,2,6,6-tetramethylpiperidine (TEMP) traps $\cdot O_2$ and displays a 1:1:1 triplet signal characteristic with a g -value of 2.0023 and hyperfine splitting constant ($aN = 171$ GHz) only under normoxia (Figure 3f, upper panel, and Figure S7a–c (Supporting Information)),

confirming that $\cdot O_2$ is produced by the Bi/BiOx lateral heterostructure in the presence of oxygen. The 5,5-dimethyl-1-pyrroline-*N*-oxide (DMPO) was used with a certain amount of methanol as quencher for $\cdot OH$ to confirm $\cdot O_2^-$ generation. The ESR signal for the Bi/BiOx displays a sextet signal only under normoxia (Figure 3f, middle panel, and Figure S7d–f (Supporting Information)), indicating that $\cdot O_2^-$ is also produced by the Bi/BiOx lateral heterostructure in the presence of oxygen. DMPO was further used to confirm $\cdot OH$ generation. The ESR signals for Bi/BiOx display a 1:2:2:1 quartet signal characteristic under both normoxic and hypoxic conditions (Figure 3f, lower panel, and Figure S7g–i (Supporting Information)), indicating that the Bi/BiOx lateral nano-heterostructure can generate $\cdot OH$ regardless of whether oxygen is present.

Chemical probes were further used to identify the ROS generation ability of the Bi/BiOx lateral nano-heterostructure. The ability of the Bi/BiOx lateral nano-heterostructure to generate singlet oxygen ($\cdot O_2$) under hypoxic and normoxic conditions was then determined. A probe molecule,

1,3-diphenylisobenzofuran (DPBF),^[26–28] was added to Bi/BiOx, and the suspension was irradiated. The samples were exposed to increasing light exposure times, and the absorbance spectra were monitored (Figure 3g). Under normoxia, the absorbance peak intensity decreased with increasing light exposure time, indicating the oxidation of DPBF by effective ¹O₂ generation (Figure 3g), whereas under hypoxia, the absorbance peak intensity was nearly unchanged, indicating the absence of ¹O₂ (Figure S8, Supporting Information). Finally, the ability of the Bi/BiOx lateral heterostructure to generate •OH was determined. Terephthalic acid (TA) was used to indirectly detect the concentration of •OH.^[29] •OH can react with terephthalic acid to produce hydroxyl terephthalic acid (HOTA), which has strong fluorescence at 425 nm. Under hypoxic conditions, the fluorescence peak gradually increased with the time of light irradiation, indicating the presence of HOTA and thus •OH (Figure 3i). A similar trend was observed under normoxic conditions (Figure S9, Supporting Information), indicating that Bi/BiOx can generate •OH independently of the presence of oxygen.

2.3. Photocatalytic Performance of H₂ Generation

H₂ gas is an endogenous gas that also exhibits significant physiological and pathological regulatory functions. It has been reported that H₂ can be utilized for the treatment of cancer.^[30,31] Methylene blue (MB)–Pt was used as an in situ chemical probe to detect the concentration of H₂ by monitoring the color change. MB can be transformed into colorless MBH₂ by reacting with H₂ in the presence of Pt nanocrystals as a catalyst.^[32,33] As shown in Figure 3h, the absorbance peak of MB at 664 nm decreased rapidly with irradiation time, indicating the effective H₂ production by Bi/BiOx lateral nano-heterostructure with 660 nm laser irradiation under hypoxia, while the absorption spectra of MB with BiNSs changed slightly under the same irradiation and hypoxic condition, indicating that no H₂ was generated by BiNSs (Figure S10, Supporting Information).

Gas chromatography was further used to detect the production of H₂ by Bi/BiOx nano-heterostructure under 660 nm laser irradiation. As shown in Figure S11 (Supporting Information), the amount of H₂ production continued to increase with the increase of illumination time, indicating that Bi/BiOx nano-heterostructure could produce H₂ effectively under 660 nm laser irradiation.

2.4. In Vitro Cell Experiments

The BiNSs and Bi/BiOx lateral nano-heterostructure underwent surface molecular engineering modification to form BiNSs and Bi/BiOx nanospheres (see the Experimental Section), namely BiNSs@PEG and Bi/BiOx@NSPs, for further biological experiments. The first requisite for a good nanomedicine is that it is biocompatible. A549 (human lung carcinoma cells), SMMC-7721 (human hepatoma cells), B16 (mouse melanoma cells), L-O₂ (human normal liver cells), HeLa (human cervical carcinoma cells), and human umbilical vein endothelial cell (HUVEC) were then systematically tested to measure the

cytotoxicity of BiNSs@PEG and Bi/BiOx@NSPs. These cells were incubated with cell culture medium containing various concentrations of BiNSs@PEG and Bi/BiOx@NSPs for 24 h, and Cell Counting Kit-8 (CCK-8) was used to measure the relative cell viabilities. The results showed that both BiNSs@PEG and Bi/BiOx@NSPs had no obvious cytotoxic effect on any of the six cell types at concentrations up to 100 μg mL⁻¹, indicating the potential safety and good biocompatibility of BiNSs@PEG and Bi/BiOx@NSPs (Figure 4a and Figure S14 (Supporting Information)).

The photocatalytic ROS and H₂ generation performance of Bi/BiOx@NSPs were also tested, indicating that the polymer coating had little influence on the photocatalytic performance of the Bi/BiOx lateral nano-heterostructure (Figure S12, Supporting Information). In view of the excellent ROS generation ability of Bi/BiOx@NSPs by the action of 660 nm light under both normoxia and hypoxia, the effect of in vitro PDT action on oxidative stress of Bi/BiOx@NSPs was evaluated. Intracellular ROS levels were measured using 2',7'-dichlorofluorescein diacetate (DCFH-DA), and the results demonstrated that Bi/BiOx@NSPs could generate free radicals and cause oxidative stress under both normoxic and hypoxic conditions (Figure 4b). Additionally, we determined the cytotoxicity of Bi/BiOx@NSPs using acridine orange/propidium iodide (AO/PI) to differentiate between the live and dead cells. SMMC-7721 cells were gradually killed by Bi/BiOx@NSPs (Figure 4c) upon irradiation at 660 nm, and the CCK-8 assay was used to test the relative cell viabilities (Figure 4d). However, BiNSs@PEG could only generate little free radicals upon irradiation with 660 nm under normoxic conditions (Figures S15–S17, Supporting Information). Annexin V–fluorescein isothiocyanate (FITC)/PI staining analysis indicated that the principal reason for the death of SMMC-7721 cells was apoptosis (Figure 4e). These results indicate the potential applications of PDT for Bi/BiOx@NSPs in clinical cancer therapy.

The intracellular DNA damaging activity of Bi/BiOx@NSPs was analyzed using a γH2AX foci analysis. γH2AX is a DNA double-strand break marker that can create γH2AX foci at or near the DNA damage site. The green fluorescence signal of γH2AX foci in Bi/BiOx@NSPs was evident in both normoxic and hypoxic microenvironments, suggesting that Bi/BiOx@NSPs had destructive DNA activity in the live cells (Figure 5a), while the BiNSs@PEG group could only generate little green fluorescence under hypoxic condition, indicating BiNSs@PEG had limited damaging to DNA in hypoxic cancer cells (Figure S18, Supporting Information).

Glutathione (GSH) in the living cells plays a major role in neutralizing the destructive effects of cell-damaging free radicals. The consumption of GSH can disrupt the intracellular redox balance and initiate oxidative stress. GSH can be depleted by the •OH generated from Bi/BiOx@NSPs under 660 nm light, and Ellman's reagent was used to examine the GSH depletion ability of Bi/BiOx@NSPs at various O₂ levels. The Bi/BiOx@NSPs resulted in obvious GSH depletion, and this was not significantly influenced by the amount of O₂ (Figure 5b). However, the BiNSs@PEG group could hardly deplete GSH under both normoxia and hypoxia microenvironments (Figure S19, Supporting Information). We also investigated the intracellular H₂ generation ability of BiNSs@PEG and Bi/BiOx@NSPs under

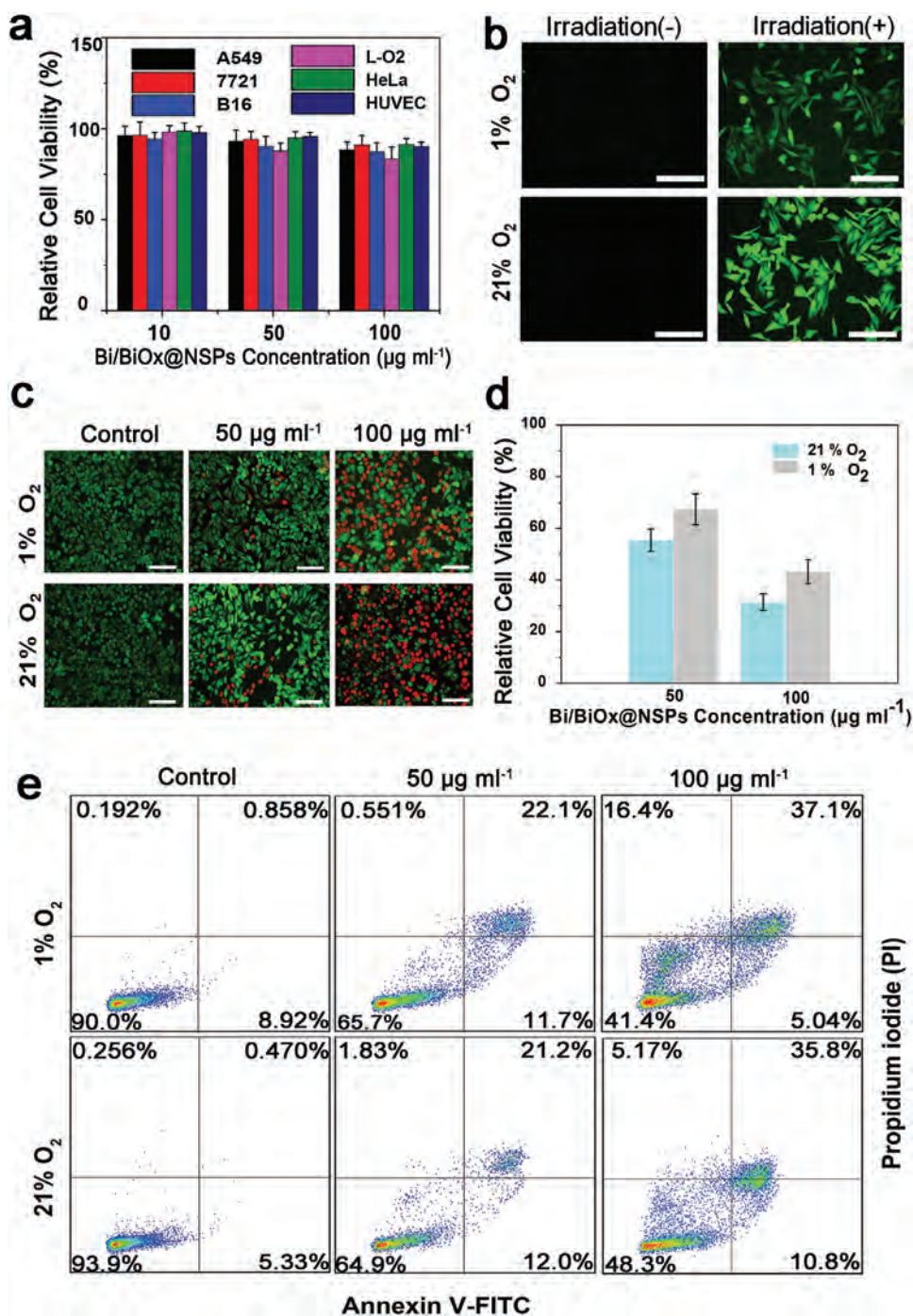


Figure 4. In vitro cell experiment. a) Relative cell viabilities of A549, SMMC-7721, B16, L-O2, HeLa, and HUVEC cells with different Bi/BiOx@NSPs concentrations (10, 50, and 100 $\mu\text{g ml}^{-1}$). b) DCFH-DA determining the oxidative-stress of SMMC-7721 cells incubated with Bi/BiOx@NSPs under 660 nm laser irradiation. c) Fluorescence images of AO (green, live cells) and PI (red, dead cells) costained SMMC-7721 cells after the addition of Bi/BiOx@NSPs and irradiation with 660 nm laser under normoxia and hypoxia. d) Phototoxicity of Bi/BiOx@NSPs to SMMC-7721 cells under normoxia and hypoxia. e) Cell apoptosis assay for SMMC-7721 cells treated with different concentrations of Bi/BiOx@NSPs under normoxia and hypoxia. Error bars, standard error ($n = 3$).

hypoxic conditions using MB probe, and found that Bi/BiOx@NSPs could release bioreductive hydrogen in cells more efficiently under 660 nm irradiation compared with BiNSs@PEG (Figure S20, Supporting Information).

The PDT-induced apoptosis of Bi/BiOx@NSPs was also confirmed by western blotting. The PDT effect could induce the degradation of Bcl-2 and the upregulation of Bax and caspase-3, which could regulate apoptosis by taking part in the apoptosis

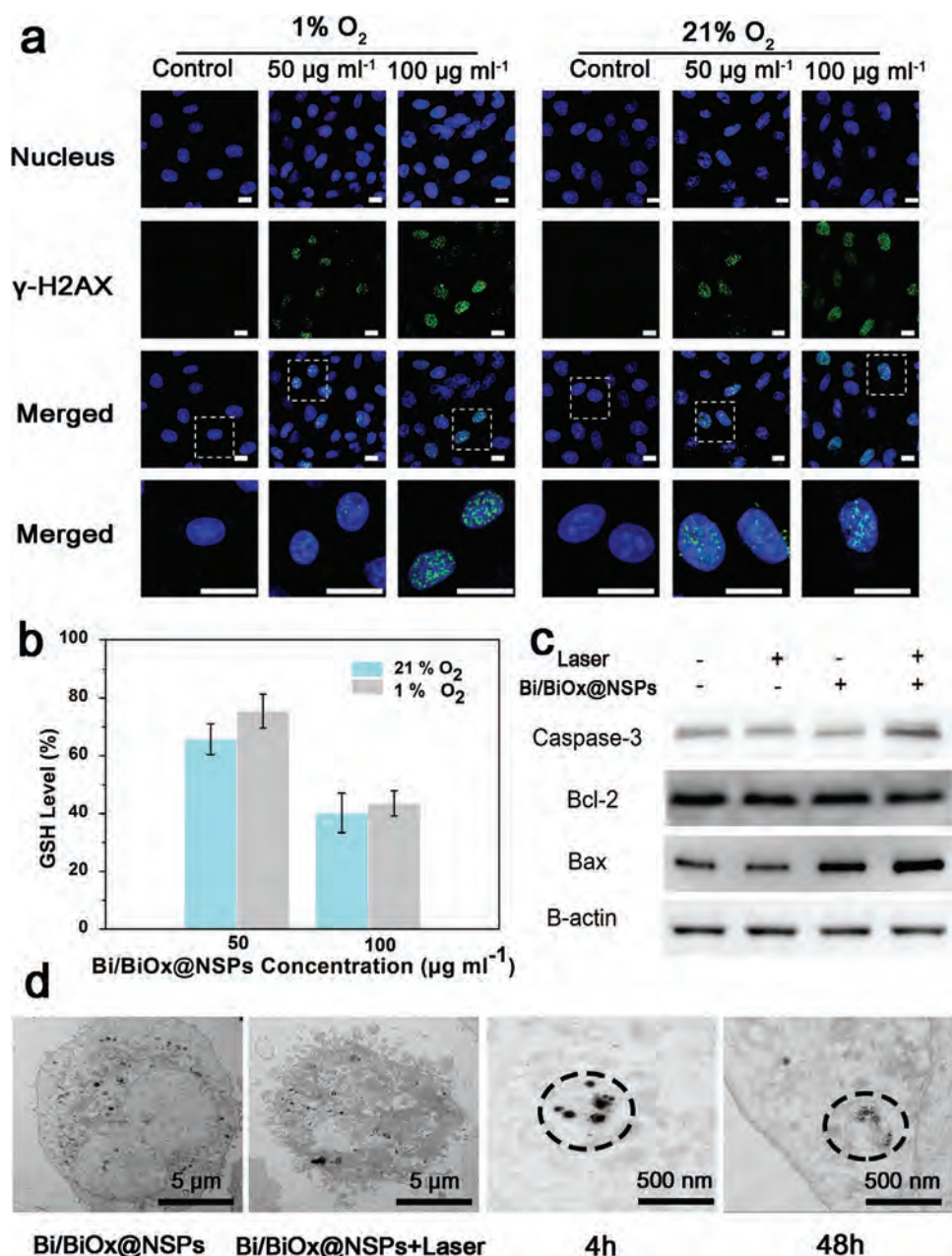


Figure 5. In vitro cell studies. a) γ -H2AX foci immunofluorescence staining of SMMC-7721 cells incubated with Bi/BiOx@NSPs and irradiated with the 660 nm laser under normoxia and hypoxia. b) GSH depletion measurement using Ellman's reagents. c) Apoptosis-related protein levels were analyzed by western blotting. d) TEM images of SMMC-7721 cells incubated with Bi/BiOx@NSPs. Error bars, standard error ($n = 3$).

pathway and signal transduction in apoptosis, resulting in the cleavage of cellular substrates and apoptosis (Figure 5c).

The intracellular biodegradation behavior of Bi/BiOx@NSPs was also studied. We used bio-TEM to directly observe structural changes in Bi/BiOx@NSPs after internalization into cancer cells for various durations (4 and 48 h) without irradiation. Bi/BiOx@NSPs were readily endocytosed and accumulated in the cytoplasm of cells after 4 h of incubation (Figure 5d). After 48 h, the biodegradation of Bi/BiOx@NSPs was clearly observed, showing a cloudy morphology without a defined structure and significant fusion of Bi/BiOx@NSPs.

2.5. In Vivo Animal Experiments

In order to reveal its potential in clinical cancer therapy, we investigated the biodistribution and tumor accumulation of BiNSs@PEG and Bi/BiOx@NSPs via aminated sulfo-cyanine7 (Cy7) labeling. BiNSs@PEG/Cy7 and Bi/BiOx@NSPs/Cy7 were injected intravenously, and full-body fluorescent imaging was employed to study their tumor accumulation. Both BiNSs@PEG/Cy7 and Bi/BiOx@NSPs/Cy7 were distributed throughout the whole body at 12 h postinjection. At 24 h postinjection, the strong fluorescence signals were observed in the tumor sites of

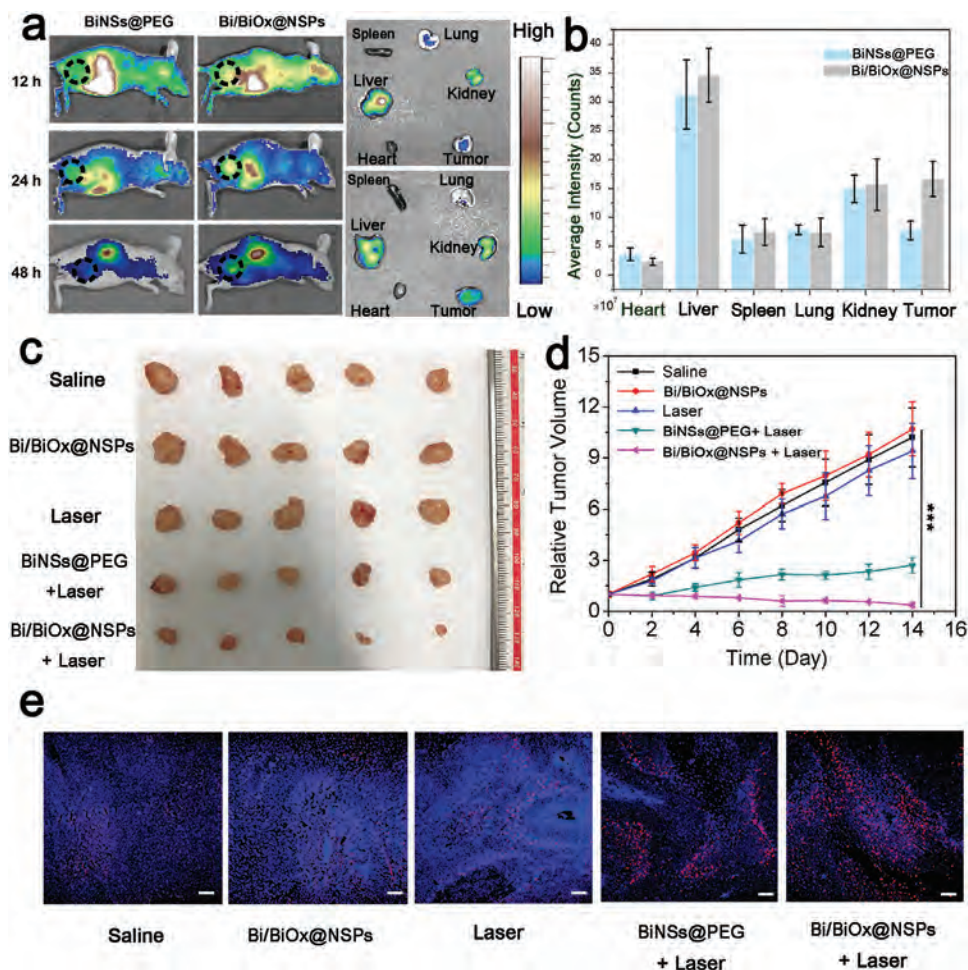


Figure 6. In vivo imaging and anticancer tumor effects of Bi/BiOx@NSPs. a) Fluorescence images of mice at 12, 24, and 48 h, and their major organs and the tumors 48 h post-irradiation. b) Semiquantitative biodistribution of Bi/BiOx@PEG and Bi/BiOx@NSPs in nude mice measured using the averaged fluorescence intensity of the organs and tumors. Error bars, standard error ($n = 3$). c) Morphology of the tumors removed from the sacrificed mice in all groups at the end point of the study. Error bars, standard error ($n = 5$). p value was calculated by a two-tailed Student's t -test ($***p < 0.001$). e) Representative fluorescence images of the TUNEL-stained tumor tissue sections derived from the mice.

both groups. At 48 h postinjection, the fluorescence intensity in both groups decreased, due to the clearance by the body as well as the biodegradability of the nanomaterial in vivo. However, the Bi/BiOx@NSPs/Cy7 group exhibited a stronger signal than the BiNSs@PEG/Cy7 group, which demonstrated the more effective in vivo targeting effect of Bi/BiOx@NSPs, owing to its improved blood circulation and enhanced permeability retention effect (Figure 6a). We also verified the in vivo tumor accumulation of the Bi/BiOx@NSPs and their in vivo targeting ability using an ex vivo investigation of the excised organs 48 h postinjection. The fluorescence signals could be observed in the liver as the Cy7 was excreted through the kidney (Figure 6a,b). Although there is a certain degree of accumulation in the liver and kidney tissues, which is an issue encountered by many other nanomedicines, the biodegradation property mentioned above could minimize the side effects and guarantee the biosafety of Bi/BiOx@NSPs.

To verify the therapeutic effect of Bi/BiOx@NSPs in vivo, SMMC-7721 liver tumors were selected from the hind flank of

the female BALB/c nude mice. The tumors from the animals in Groups 2 and 3 grew rapidly over a two-week study, indicating that treatment with either Bi/BiOx@NSPs only or laser irradiation alone had no inhibitory effect on tumor growth. A significant therapeutic effect was observed in Groups 4 and 5 (Figure 6c,d), where BiNSs@PEG or Bi/BiOx@NSPs were combined with 660 nm light irradiation, when compared to the control group. In fact, the decrease in the tumor volume in Group 5 was greater than that in Group 4, indicating that an improved therapeutic effect was achieved by the Bi/BiOx@NSP-based PDT strategy. The better PDT efficiency of the Bi/BiOx@NSPs compared to that of BiNSs@PEG could be attributed to three factors. First, the Bi/BiOx@NSPs have a prolonged blood circulation time in the body owing to the negatively charged surface (Figure S21, Supporting Information). Second, Bi/BiOx@NSPs have a reduced size and surface charge under an acidic tumor microenvironment for better tumor tissue penetration. Third, the unique nano-heterostructure endowed Bi/BiOx@NSPs with excellent ROS generation for better PDT efficacy under hypoxic conditions.

Apoptosis in tumors was further analyzed by terminal deoxynucleotidyl transferase-mediated nick-terminal marker (TUNEL) assay. Only a few TUNEL-positive cells (green) were observed in the saline, Bi/BiOx@NSPs only, or laser only groups, while a significant number of TUNEL-positive apoptotic cells were observed in the Bi/BiOx@NSPs/laser group, indicating that Bi/BiOx@NSP-mediated PDT can activate apoptosis, which leads to intratumoral cell death (Figure 6e). In addition, hematological and blood biochemical analyses and body weight data demonstrated that administering Bi/BiOx@NSPs and laser treatment for 7 days caused no significant toxicity (Figure S22a,b, Supporting Information). To further evaluate the *in vivo* toxicity of the Bi/BiOx@NSPs with the laser, the major organs of the mice were stained with hematoxylin and eosin for histological analysis. No noticeable morphological changes were observed in the normal tissues, indicating that the Bi/BiOx@NSPs and the laser had no observable toxicity or side effects on the healthy tissues (Figure S22c, Supporting Information).

3. Conclusions

PDT is as an emerging platform with specific spatiotemporal selectivity and minimal invasiveness that has been clinically approved for the treatment of several types of malignant cancer. However, poor biocompatibility and biodegradability, together with the relatively low ROS generation ability of conventional photosensitizers, hinders the widespread clinical use of PDT. Recently, a series of novel 2D-material-based PDT photosensitizers, including graphene, MXene, and phosphorene, with excellent PDT performances were developed, benefiting from the extraordinary physicochemical properties of 2D materials. The PDT performance parameters for the classic inorganic PDT sensitizers and 2D inorganic PDT sensitizers are summarized and compared in Table S1 (Supporting Information). However, the therapeutic efficacy of PDT was greatly suppressed by the hypoxic tumor microenvironment, as ROS generation during the PDT process is highly oxygen-dependent. Therefore, an oxygen-independent ROS generation strategy has become a hot topic in PDT research.

In this study, to solve the abovementioned issue, we prepared a Bi/BiOx lateral nano-heterostructure using a combined regioselective coordination and orientational oxidation method, and demonstrated its O₂-independent ROS generation ability, which could be used for hypoxic PDT treatments. In addition to the ¹O₂ generation process using an energy transfer type II PDT mechanism, a type I PDT was further activated by the electron transfer process benefiting from the Bi/BiOx lateral nano-heterostructure under 660 nm light irradiation. The underlying mechanism of the photocatalytic process was investigated thoroughly, and it was found that hydroxide ions were oxidized to •OH on the anodic valence of BiOx, while O₂ and H⁺ were reduced to O₂^{•-} and H₂ under normoxia and hypoxia, respectively, at the cathodic Fermi level of the Bi. Therefore, it was found that the Bi/BiOx lateral nano-heterostructure can generate ROS under 660 nm light irradiation in both normoxic and hypoxic tumor microenvironments. Furthermore, *in vitro* and *in vivo* experiments demonstrated that the Bi/BiOx lateral

nano-heterostructure has excellent tumor ablation capability as well as superior biocompatibility and tumor targeting after surface molecular engineering modifications. Such a novel therapeutic nanoplatform with ultrahigh PDT efficiency under hypoxic tumor conditions and with inherent biosafety promises to advance the future of customized precision medical treatments.

4. Experimental Section

Materials: Bulk Bi powder was purchased from Sigma-Aldrich and stored in a dark, nitrogen-atmosphere glove box. N-methyl-2-pyrrolidone (NMP) and ethanol (99.5%, anhydrous) were purchased from Aladdin Reagents. Titanium *p*-aminobenzene sulfonate (Ti-Aryl-NH₂) and HOOC-PEG-COOH with a molecular weight of 5 kDa were both purchased from Yarebio Co., Ltd. (Shanghai, China). The TEMP, DMPO, DPBF, MB, and TA were all purchased from Sigma-Aldrich. Colloidal Pt (99.9%; 2 wt%) was purchased from Jingkang Bioengineering Co., Ltd. (Shanghai, China), and the autoclave was purchased from Shanghai Yushen Instrument Co., Ltd. (Shanghai, China). The centrifuge used in this study was an HR20M, with a rotor radius (*R*) of 9.4 cm, produced by Herexi Instrument & Equipment Co., Ltd. (Hunan, China). The relationship between the relative centrifugal force (*G*) and revolutions per minute (rpm) was $G = 1.11 \times 10^{-5} (R) \times (\text{rpm})^2$, where *R* is the radius of the centrifuge rotor.^[34] Cy7 was purchased from Ruixibio Co., Ltd. (Xi'an, China). The AO/PI assay kit was obtained from Logos Biosystems (Anyang-si, South Korea). PBS (pH 7.4), fetal bovine serum (FBS), RPMI-1640 medium (RPMI = Roswell Park Memorial Institute), trypsin-ethylene diamine tetraacetic acid (EDTA), and penicillin/streptomycin were purchased from Gibco Life Technologies (AG, NY, USA). The DCFH-DA and trypan blue were both purchased from the Beyotime Institute of Biotechnology (Shanghai, China). Annexin V-FITC/PI apoptosis and necrosis detection kits were purchased from TransGen Biotech Co., Ltd. (Beijing, China). Primary antibodies for β-actin, Bcl-2, cyt-c, caspase-3, and the secondary antibodies were purchased from Thermo Fisher (MA, USA). The enhanced chemiluminescence detection system kit was obtained from Tanon Science & Technology (Shanghai, China). Ultrapure water (18.25 MΩ cm, 25 °C) was used to prepare all solutions. All other chemicals used in this study were of analytical reagent grade and were used without further purification. All kits used in this study were in accordance with the manufacturer's guidelines, unless otherwise stated.

Preparation of Bi/BiOx Lateral Nano-Heterostructure: The Bi/BiOx lateral nano-heterostructure was fabricated using a two-step "regioselective coordination" and subsequent "orientational oxidation" method (Figure 1a). Briefly, 1 g of Bi powder was dispersed in 400 mL NMP bubbled with N₂ for 30 min in a 500 mL autoclave, followed by a hydrothermal reaction at 200 °C for 24 h under N₂. The autoclave was cooled naturally after centrifuging for 30 min at 3000 rpm to remove the unexfoliated Bi powder, and the supernatant was centrifuged at 18 000 rpm for 5 min with 30 mL ethanol 3 times to purify the product. To promote the colloidal stability of the BiNSs, 30 mL of the as-prepared suspension was poured into a 50 mL glass vial and stirred with 50 mg Ti-Aryl-NH₂ for 3 h. This was done to allow the lone electron pair of the surficial Bi atoms to selectively coordinate with the empty d orbitals of the Ti atoms in Ti-Aryl-NH₂, leaving the dangling bonds of the BiNSs edge alone. After the reaction, the free Ti-Aryl-NH₂ was removed by centrifuging the suspension at 18 000 rpm for 5 min. The precipitate was collected and redispersed in 100 mL NMP with saturated O₂. It was then transferred into a 150 mL autoclave for another 12 h hydrothermal reaction to obtain the BiNSs that had an oxidized outer shell, as the dissolved O₂ reacted with the edge dangling bonds of the BiNSs forming the Bi/BiOx nano-heterostructure. After centrifuging for 30 min at 3000 rpm to remove the agglomerated large particles, the supernatant was further centrifuged for another 30 min at 18 000 rpm to yield the purified Bi/BiOx lateral nano-heterostructure. Thereafter,

the as-prepared Bi/BiOx lateral nano-heterostructure was washed with 30 mL ethanol by centrifuging twice for 5 min at 18 000 rpm, 2 times, and it was then redispersed into 30 mL ethanol. The concentration of the Bi/BiOx lateral nano-heterostructure suspension was determined to be 1.6 mg mL⁻¹ with a total yield of 4.8%, using inductively coupled plasma mass spectroscopy (ICP-MS).

Surface Modification of the Bi/BiOx Lateral Nano-Heterostructure: The HOOC-PEG-COOH was further coupled to Ti-Aryl-NH₂ with 1-(3-dimethylaminopropyl)-3-ethylcarbodiimide for surface modifications of the Bi/BiOx, which not only improved the aqueous dispersibility and biocompatibility of Bi/BiOx lateral nano-heterostructures in the physiological media, but also enhanced the blood circulation time and tumor penetration depth. In brief, 20 mg of the Bi/BiOx heterostructure was dispersed in 100 mL of chloroform containing 100 mg of predissolved HOOC-PEG-COOH. After 10 min of probe sonication, the chloroform was removed using low-temperature vacuum rotary evaporation. The obtained Bi/BiOx@NSPs were then dispersed in water, centrifuged at 18 000 rpm for 30 min, and washed with deionized (DI) water 3 times to remove the unbound HOOC-PEG-COOH. The final Bi/BiOx@NSP samples were resuspended in 10 mL PBS solution and stored at 4 °C until future use. For *in vivo* fluorescent imaging, 10 mg Cy7 was mixed with 1 mg BiNSs@PEG or Bi/BiOx@NSPs and then stirred at room temperature for 4 h. Free Cy7 was removed by centrifuging the suspension at 15 000 rpm for 5 min, and then the precipitate was harvested and redispersed in DI water.

Characterization Methods: TEM and high-resolution TEM (HRTEM) were employed to characterize the morphology and elemental composition of the BiNSs and Bi/BiOx nano-heterostructures. SAED and EDS were performed at 300 kV using FEI Tecnai G² F30 field-emission TEM equipment. AFM was employed to characterize the morphology and height of the Bi/BiOx using an ICON Bruker system in the tapping mode, and the samples were dispersed on Si/SiO₂ substrates using a drop-casting method and the images (512 pixels per line) were recorded at a scan rate of 1.79 Hz. XPS was performed to analyze the surface chemicals of the Bi/BiOx on the ULVAC PHI 5000 VersaProbe II using an Al K_α (λ = 0.83 nm, hν = 1486.7 eV). X-ray source was operated at 23.5 W, and the data were analyzed using MultiPak Version 9.0 software. Raman spectra were acquired using a HORIBA JY LabRAM HR Evolution Raman microscope equipped with a 514 nm argon ion laser as the excitation source. UV-vis spectroscopy was performed using a PerkinElmer LAMBDA 750 spectrophotometer to measure the optical absorbance of Bi/BiOx in the 200–1100 nm range, using prealigned tungsten-halogen and deuterium lamps as the incident light source. The concentration of the Bi/BiOx lateral nano-heterostructure suspension was determined using ICP-MS (Agilent 7700).

Measurement of ROS Generation: The singlet oxygen generation ability of the samples was investigated using ESR measurements on a Bruker A300 X-band ESR spectrometer. Dispersion of the samples (BiNSs or Bi/BiOx, 50 μg mL⁻¹) and spin trap molecules (TEMP, DMPO, 10 × 10⁻³ M) were mixed in sealed vials and bubbled with nitrogen (hypoxia) or air (normoxia) for 30 min, and then exposed to 660 nm laser light irradiation for 1 min at a light density of 0.1 W cm⁻². Finally, the dispersions were transferred to a quartz capillary tube, and the ESR signals were tested at room temperature in a vacuum.

The singlet oxygen generation ability of the sample was investigated using DPBF measurements performed on a Hitachi UH4150 ultraviolet-visible-near-infrared (UV-vis-NIR) spectrophotometer. The samples (BiNSs or Bi/BiOx, 50 μg mL⁻¹) were dispersed with DPBF's dehydrated ethanol suspension (40 μg mL⁻¹) in sealed vials, and bubbled with nitrogen (hypoxia) or air (normoxia) for 30 min. The dispersions were then transferred to a quartz capillary tube and irradiated with 660 nm laser light for 1 min at a light density of 0.1 W cm⁻², the light was then shut off and UV measurements were conducted, then the light was turned on to irradiate the suspension for 1 min. This cycle was performed for 20 min and the peak intensity was recorded and compared at 410 nm.

•OH interact with TA to produce HOTA, which had a strong fluorescence at 425 nm after excitation with 315 nm incident light. The generation of •OH was detected by measuring the intensity of the

HOTA fluorescence peak using a fluorescence spectrophotometer. The standard curve range was 0.5–10 μg mL⁻¹, and the fluorescence intensity showed a linear increase with the concentration of HOTA (Figure S10a, Supporting Information). As the TA could be dissolved in an alkali solution, the NaOH additive dissolved in the deionized water changed the pH to 9. The TA (1 mg) was added to a 200 mL alkali solution and stirred for 10 min to form the TA reagent (with a TA concentration of 5 μg mL⁻¹). Then, 1 μL Bi/BiOx (200 μg mL⁻¹) was dispersed in a 1.5 mL TA solution to prepare the testing sample (with a Bi/BiOx concentration of 0.13 μg mL⁻¹). The fluorescence spectra range for the samples was 405–480 nm under an excitation wavelength of 315 nm.

Measurement of H₂ Generation: An MB-Pt probe was employed to detect the H₂ concentration using the UV-vis absorbance spectra. MB reacted with H₂ to produce colorless MBH₂ in the presence of a Pt catalyst. The standard curve ranged from 0.5 to 15 μg mL⁻¹, in which the absorption peak intensity increased linearly with the MB solution (Figure S10b, Supporting Information). Briefly, 5 mg MB was added to 1000 mL deionized water ventilated with N₂ gas to produce the MB solution (with a MB concentration of 5 μg mL⁻¹). Then, 0.1 g colloidal Pt (2 wt%) was added to the MB solution to produce the MB-Pt reagent (with a Pt concentration of 2 μg mL⁻¹). Then, 1 μL Bi/BiOx (200 μg mL⁻¹) was dispersed in a 1.5 mL MB-Pt reagent to prepare the testing sample (with a Bi/BiOx concentration of 0.13 mL⁻¹). The concentration of Bi/BiOx NSPs was sufficiently small to avoid any effect on the absorption spectra of the pure MB-Pt reagent. Methanol (0.1 mL) was added as a trapping agent for •OH to avoid the affection of •OH. The wavelength used in the detection of H₂ was 400–950 nm, and a strong absorption peak at 664 nm was detected for pure MB. Upon reaction with hydrogen under the catalysis of Pt nanocrystals, the MB was rapidly reduced to colorless MBH₂, and the reduction of the 664 nm absorbance peak was linearly related to the amount of H₂.

The H₂ production reaction was further confirmed using photocatalytic activity experiments. Bi/BiOx (5 mg) was dispersed in a 15% v/v solution of triethanolamine in 40 mL of water in a 50 mL Pyrex reactor. The mixture was thoroughly ventilated with N₂ and stirred continuously. The glass reactor was connected to a gas chromatographic assembly (GC-14C, Shimadzu, Japan, TCD); N₂ was used as carrier gas and it was irradiated under a 660 nm laser (1 W cm⁻²). The production of H₂ was measured every 0.5 h for 4 h.

Cell Culture Assays: A549, SMMC-7721, B16, L-O2, HeLa, and HUVECs were obtained from the American Type Culture Collection. They were all cultured in normal RPMI-1640 medium with 10% FBS and 1% penicillin/streptomycin at 37 °C with 5% CO₂.

In Vitro Toxicity and Safety Studies: A549, SMMC-7721, B16, L-O2, HeLa, and HUVEC cells were seeded at a density of 8000 cells per well in 96-well plates and incubated overnight. The cells were then incubated with BiNSs@PEG and Bi/BiOx@NSPs at different concentrations (0, 10, 50, 100, and 200 μg mL⁻¹) for 24 h (n = 5). The culture medium was replaced with CCK-8 reagent, and the cells were incubated for an additional 1 h at a predetermined time. The absorbance at 450 nm was measured using a microplate reader (ELx808; BioTek). Untreated cells were used as the control group.

In Vitro PDT Study: The SMMC-7721 cells were incubated with BiNSs@PEG and Bi/BiOx@NSPs (0, 50, and 100 μg mL⁻¹) for 4 h at 37 °C under different conditions (with 21% O₂ or 1% O₂) and then irradiated using a 660 nm laser (0.1 W cm⁻²) for 10 min. The area of each well was fully covered by a laser spot. After additional incubation for 12 h, the residual materials were thoroughly removed by rinsing 3 times with PBS, and the relative cell viabilities were then measured using the CCK-8 assay. For the AO/PI dyeing experiment, the cells were stained with AO/PI, and fluorescence was observed using a fluorescence microscope.

DCFH-DA was used to measure intracellular free radicals and oxidative stress under both normoxic and hypoxic conditions. The SMMC-7721 cells were incubated with BiNSs@PEG and Bi/BiOx@NSPs (100 μg mL⁻¹) for 4 h at 37 °C under different conditions (with 21% O₂ or 1% O₂), and the medium was removed, and they were washed with PBS 3 times. Then, the cells were incubated with DCFH-DA for 10 min at

37 °C in the dark and then irradiated with a 660 nm laser (0.1 W cm⁻²) for 10 min. The cells were washed 3 times with PBS. The fluorescence of the activated DCFH-DA was observed using a fluorescence microscope.

Annexin V-FITC/PI Double-Staining Assay: SMMC-7721 cells were incubated with different concentrations of BiNSs@PEG and Bi/BiOx@NSPs under normoxia and hypoxia and irradiated with a 660 nm laser at a power density of 0.1 W cm⁻². After another 12 h of incubation, SMMC-7721 cells were harvested, washed, and resuspended in PBS. Cells were determined with a TransDetect Annexin V-FITC/PI Cell Apoptosis Detection Kit (Transgen Biotech), according to the manufacturer's protocol, and analyzed using a DxFLEX flow cytometer (Beckman Coulter).

γ-H2AX Foci Assay: The SMMC-7721 cells were incubated on coverslips in a 6-well plate for 24 h, and then incubated with 50 or 100 μg mL⁻¹ of BiNSs@PEG and Bi/BiOx@NSPs for 4 h and irradiated with a 660 nm NIR laser light for 5 min with a light density of 0.1 W cm⁻². After 4 h of irradiation, the cells were fixed with 4% paraformaldehyde for 10 min. These cells were then permeabilized with 0.2% Triton X-100 for 10 min and incubated in 3% bovine serum albumin in PBS buffer for 30 min. The cells were then incubated with monoclonal antibodies against γ-H2AX overnight at 4 °C. Afterward, they were incubated with FITC-labeled secondary antibody for 1 h and then stained with 2-(4-aminodiphenyl)-6-indolecarbamidine dihydrochloride (DAPI) for 10 min.

Cellular GSH and Apoptosis-Associated Protein Assay: SMMC-7721 cells were seeded in a 6-well plate and incubated with BiNSs@PEG and Bi/BiOx@NSPs (0, 50, and 100 μg mL⁻¹) for 4 h under different conditions (with 21% O₂ or 1% O₂) and then irradiated using a 660 nm laser (0.1 W cm⁻²) for 10 min. Then, 200 μL of Triton-X-100 lysis buffer was added to lyse the cells. The lysates were then centrifuged, and the supernatant was mixed with 0.5 × 10⁻³ M 5,5'-dithiobis-(2-nitrobenzoic acid) (DTNB). Absorbance was measured at 405 nm using a microplate reader. Apoptosis-associated proteins were extracted with radioimmunoprecipitation assay (RIPA) lysis buffer and detected by western blotting.

Measurement of Intracellular Hydrogen Release: SMMC-7721 cells at the density of 8000 cells per well were plated in a 96-well plate and cultivated under 1% O₂. After incubation for 24 h, the medium was replaced with fresh medium containing the MB probe. After incubation for 2 h, the medium was replaced with fresh one containing the BiNSs@PEG and Bi/BiOx@NSPs at the concentration of 100 μg mL⁻¹. After incubation for 4 h, the 96-well plate was irradiated with 660 nm NIR laser light for 5 min with a light density of 0.1 W cm⁻². After 1 h, the plate was monitored using the Bio-Tek multimode microplate reader (absorption wavelength: 664 nm).

Cell Uptake Study: The uptake of the Bi/BiOx@NSP cells was investigated using transmission electron microscopy. The SMMC-7721 cells were incubated with 50 μg mL⁻¹ of Bi/BiOx@NSPs for 4 or 48 h. These cells were fixed with glutaraldehyde for 4 h and then fixed with 2% osmium tetroxide for 1 h. The cells were dehydrated in a series of graded ethanol solutions and embedded in agar 100 epoxy resin. The cells were then cut with a diatom diamond knife on an LBK ultramicrotome Leica UCT. Finally, the sections were examined using a Tecnai G2 TEM instrument (FEI, Netherlands).

In Vivo Anticancer Studies: Female BALB/c (nu/nu) mice (5 weeks old) were purchased from the Guangdong Medical Laboratory Animal Center (Guangzhou, China). All animal experiments were conducted in compliance with the guidelines from and approved by the Animal Welfare and Research Ethics Committee of Shenzhen University (ID: 2017003). The tumor model was generated by injecting SMCC-7721 cells (5 × 10⁶ cells per mouse) in the right hind flank of each mouse. After the average tumor volume exceeded 100 mm³, the mice were randomly divided into five groups (*n* = 5 in each group) that were intravenously administered the following treatments: 100 μL of saline (Group 1, control); 5 mg kg⁻¹ Bi/BiOx@NSPs without laser irradiation (Group 2); saline with laser irradiation (Group 3); 5 mg kg⁻¹ BiNSs@PEG with irradiation (Group 4); and 5 mg kg⁻¹ Bi/BiOx@NSPs with irradiation (Group 5). 24 h postinjection, the mice in Groups 3, 4, and 5 were anesthetized with pentobarbital sodium and the entire region of the

tumor was irradiated with a 660 nm laser (0.1 W cm⁻²) for 10 min. The tumor volume was calculated according to the formula: tumor volume = 1/2 × tumor length × tumor width². V₀ was the initial tumor volume in the treatment, and the relative tumor volumes were calculated as V/V₀. At the end of the experiment (Day 14), all mice were euthanized, and the tumors were collected and detected using the TUNEL method.

In Vivo Biodistribution: For the in vivo fluorescence imaging experiments, the BALB/c (nu/nu) mice with SMCC-7721 tumors were divided into two groups (*n* = 3 in each group). The mice were then injected via their tails with 100 μL BiNSs@PEG/Cy7 (1 mg mL⁻¹) and Bi/BiOx@NSPs/Cy7 (1 mg mL⁻¹), respectively. An IVIS Spectrum (PerkinElmer) was used to obtain in vivo images of the mice at 12, 24, and 48 h postinjection. A 740 nm wavelength light was used as the excitation source, and 760 nm emitted light was detected. Afterward, mice were sacrificed, and the tumor, heart, liver, spleen, lung, and kidney were collected. The fluorescence in all organs was acquired using the IVIS Spectrum (PerkinElmer) imaging system.

In Vivo Blood Circulation: The pharmacokinetics of Bi/BiOx@NSPs were determined using both fluorescence and inductively coupled plasma-atomic emission spectroscopy (ICP-AES) measurements. First, BALB/c (nu/nu) mice bearing SMCC-7721 tumors were injected via their tails with 100 μL Bi/BiOx@NSPs/Cy7 (1 mg mL⁻¹). The Cy7 fluorescence intensity of the Bi/BiOx@NSPs/Cy7 in the blood of the SMMC-7721-tumor-bearing Balb/c mice was determined at different time points postinjection. Second, BALB/c (nu/nu) mice bearing SMCC-7721 tumors were injected via their tails with 100 μL Bi/BiOx@NSPs (1 mg mL⁻¹). The bismuth concentrations of the Bi/BiOx@NSPs in the blood of the SMMC-7721-tumor-bearing Balb/c mice were determined at different time points postinjection. The collected samples were digested with HNO₃ for the ICP-MS measurements to quantify the bismuth concentration.

Statistical Analysis: All data were reported as the mean ± s.d.; *n* = 3 for all in vitro, in vivo biodistribution and blood circulation experiments. *n* = 5 for in vivo anticancer studies. *p* values were calculated using a two-tailed Student's *t* test to test the significance of the difference between sample groups using GraphPad Prism 8 Software. Statistical values are indicated according to the following scale: * *p* < 0.05, ** *p* < 0.01, and *** *p* < 0.001.

Supporting Information

Supporting Information is available from the Wiley Online Library or from the author.

Acknowledgements

The authors acknowledge the support from Instrumental Analysis Center of Shenzhen University (Xili Campus). Partial support from The Institute for Lasers, Photonics and Biophotonics at The University at Buffalo is also acknowledged. This work was financially supported by the National Natural Science Foundation of China (Grant Nos. U1801254, 61961136001, H.Z.; Grant No. U1803128, M.Q.), the State Key Research Development Program of China (Grant No. 2019YFB2203503, H.Z.), the Taishan Scholar Project of Shandong Province (Grant No. tsqn201909054, M.Q.), the Science and Technology Innovation Commission of Shenzhen (Grant Nos. KQTD2015032416270385, JCYJ20150625103619275, H.Z.; Grant No. JCYJ20180305124854790, M.Q.; Grant No. JCYJ20180507181817604, S.B.) and the Natural Science Foundation of Guangdong Province (Grant No. 2018A030310500, M.Q.).

Conflict of Interest

The authors declare no conflict of interest.

Author Contributions

M.Q., D.W., H.H., and T.Y. contributed equally to this work. M.Q., D.W., H.H., and T.Y. performed most of the experiments, analyzed data, and wrote the paper. H.L.K. critiqued the paper and contributed to writing. P.N.P. and H.Z. guided the research, reviewed and improved the paper. W.B., B.Z., Z.X., N.X., Z.W., C.G., and Q.W. performed some experiments. M.G., L.L., and S.B. analyzed some data. P.N.P. and H.Z. are the guarantors of this work, have full access to all of the data in the study, and take responsibility for the integrity of the data and the accuracy of the data analysis.

Data Availability Statement

The data that support the findings of this study are available from the corresponding author upon reasonable request.

Keywords

2D materials, bismuthene, hypoxia, lateral nano-heterostructures, photodynamic therapy

Received: April 3, 2021
Revised: September 2, 2021
Published online:

- [1] World Health Organization, https://www.who.int/health-topics/cancer#tab=tab_1 (accessed: September 2021).
- [2] P. N. Prasad *Introduction to Nanomedicine and Nanobioengineering*, John Wiley & Sons, Hoboken, NJ, USA **2012**.
- [3] D. Dolmans, D. Fukumura, R. K. Jain, *Nat. Rev. Cancer* **2003**, *3*, 380.
- [4] J. C. Ge, M. H. Lan, B. J. Zhou, W. M. Liu, L. Guo, H. Wang, Q. Y. Jia, G. L. Niu, X. Huang, H. Y. Zhou, X. M. Meng, P. F. Wang, C. S. Lee, W. J. Zhang, X. D. Han, *Nat. Commun.* **2014**, *5*, 4596.
- [5] N. M. Idris, M. K. Gnanasammandhan, J. Zhang, P. C. Ho, R. Mahendran, Y. Zhang, *Nat. Med.* **2012**, *18*, 1580.
- [6] V. H. Fingar, T. J. Wieman, S. A. Wiehle, P. B. Cerrito, *Cancer Res.* **1992**, *52*, 4914.
- [7] J. Kim, H. R. Cho, H. Jeon, D. Kim, C. Song, N. Lee, S. H. Choi, T. Hyeon, *J. Am. Chem. Soc.* **2017**, *139*, 10992.
- [8] Y. Liu, Y. Liu, W. Bu, C. Cheng, C. Zuo, Q. Xiao, Y. Sun, D. Ni, C. Zhang, J. Liu, *Angew. Chem., Int. Ed.* **2015**, *54*, 8105.
- [9] J. Liu, P. Du, H. Mao, L. Zhang, H. Ju, J. Lei, *Biomaterials* **2018**, *172*, 83.
- [10] B. Tian, C. Wang, S. Zhang, L. Z. Feng, Z. Liu, *ACS Nano* **2011**, *5*, 7000.
- [11] S. G. Shi, X. L. Zhu, Z. X. Zhao, W. J. Fang, M. Chen, Y. Z. Huang, X. L. Chen, *J. Mater. Chem. B* **2013**, *1*, 1133.
- [12] G. Song, C. Liang, H. Gong, M. Li, X. Zheng, L. Cheng, K. Yang, X. Jiang, Z. Liu, *Adv. Mater.* **2015**, *27*, 6110.
- [13] C. Liu, B. Liu, J. Zhao, Z. Di, D. Chen, Z. Gu, L. Li, Y. Zhao, *Angew. Chem., Int. Ed.* **2020**, *59*, 2634.
- [14] X. Dai, T. Du, K. Han, *ACS Biomater. Sci. Eng.* **2019**, *5*, 6342.
- [15] E. R. Swy, A. S. Schwartz-Duval, D. D. Shuboni, M. T. Latourette, C. L. Mallet, M. Parys, D. P. Cormode, E. M. Shapiro, *Nanoscale* **2014**, *6*, 13104.
- [16] H. Lusic, M. W. Grinstaff, *Chem. Rev.* **2013**, *113*, 1641.
- [17] X. Yu, A. Li, C. Zhao, K. Yang, X. Chen, W. Li, *ACS Nano* **2017**, *11*, 3990.
- [18] J. Chen, J. Ding, Y. Wang, J. Cheng, S. Ji, X. Zhuang, X. Chen, *Adv. Mater.* **2017**, *29*, 1701170.
- [19] Q. Zhou, S. Shao, J. Wang, C. Xu, J. Xiang, Y. Piao, Z. Zhou, Q. Yu, J. Tang, X. Liu, Z. Gan, R. Mo, Z. Gu, Y. Shen, *Nat. Nanotechnol.* **2019**, *14*, 799.
- [20] R. Tong, H. H. Chiang, D. S. Kohane, *Proc. Natl. Acad. Sci. USA* **2013**, *110*, 19048.
- [21] K. Trentelman, *J. Raman Spectrosc.* **2009**, *40*, 585.
- [22] Y. Nosaka, A. Y. Nosaka, *Chem. Rev.* **2017**, *117*, 11302.
- [23] M. Buchalska, M. Pacia, M. Kobielski, M. Surówka, E. Świątek, E. Właźlak, K. Szaciłowski, W. Macyk, *J. Phys. Chem. C* **2014**, *118*, 24915.
- [24] Y. Cai, G. Zhang, Y. Zhang, *Sci. Rep.* **2015**, *4*, 6677.
- [25] Q. Zhou, Q. Chen, Y. Tong, J. Wang, *Angew. Chem., Int. Ed.* **2016**, *55*, 11437.
- [26] W. Piao, K. Hanaoka, T. Fujisawa, S. Takeuchi, T. Komatsu, T. Ueno, T. Terai, T. Tahara, T. Nagano, Y. Urano, *J. Am. Chem. Soc.* **2017**, *139*, 13713.
- [27] H. Wang, X. Yang, W. Shao, S. Chen, J. Xie, X. Zhang, J. Wang, Y. Xie, *J. Am. Chem. Soc.* **2015**, *137*, 11376.
- [28] R. Lv, D. Yang, P. Yang, J. Xu, F. He, S. Gai, C. Li, Y. Dai, G. Yang, J. Lin, *Chem. Mater.* **2016**, *28*, 4724.
- [29] Y. Nakabayashi, Y. Nosaka, *Phys. Chem. Chem. Phys.* **2015**, *17*, 30570.
- [30] M. Dole, F. R. Wilson, W. P. Fife, *Science* **1975**, *190*, 152.
- [31] P. Zhao, Z. Jin, Q. Chen, T. Yang, D. Chen, J. Meng, X. Lu, Z. Gu, Q. He, *Nat. Commun.* **2018**, *9*, 4241.
- [32] T. Seo, R. Kurokawa, B. Sato, *Med. Gas Res.* **2012**, *2*, 1.
- [33] M. Zhu, Y. Osakada, S. Kim, M. Fujitsuka, T. Majima, *Appl. Catal., B* **2017**, *217*, 285.
- [34] V. P. Dole, G. C. Cotzias, *Science* **1951**, *113*, 552.